

Experimental observation of the acoustic \mathbb{Z}_2 Weyl semimetallic phase in synthetic dimensionsFarzad Zangeneh-Nejad  and Romain Fleury ^{*}*Laboratory of Wave Engineering, School of Electrical Engineering, EPFL, Station 11, 1015 Lausanne, Switzerland*

(Received 8 May 2020; revised 7 August 2020; accepted 9 August 2020; published 27 August 2020)

Scalar waves such as airborne sound lack an intrinsic spin degree of freedom, making the realization of sonic \mathbb{Z}_2 topological phases based on spin degeneracy challenging. Here, we demonstrate the relevance of synthetic dimensions and higher-dimensional topological physics for exploring topological phases based on acoustic pseudo-spin with exact Kramers degeneracy. Interestingly, we find that a carefully designed two-band one-dimensional Hamiltonian with two additional phason degrees of freedom can enter a \mathbb{Z}_2 semimetallic phase with nonzero topological invariants carried by pairs of Weyl points in a three-dimensional synthetic momentum space. Taking advantage of the high localization of sonic quasibound states, embedded in the modal continuum of a one-dimensional acoustic waveguide, we implement a \mathbb{Z}_2 topological Weyl system and experimentally observe its signature in far-field sound scattering experiments. Our findings establish sonic quasibound states in continuum as a fertile ground for exploring higher dimensional Weyl physics in scattering media, and provide a viable experimental path to study spin-related topological effects in acoustics.

DOI: [10.1103/PhysRevB.102.064309](https://doi.org/10.1103/PhysRevB.102.064309)**I. INTRODUCTION**

Electronic quantum spin Hall insulators [1,2], characterized by a \mathbb{Z}_2 topological invariant [3], are phases of matter with a nonvanishing spin-Hall conductance. In contrast to ordinary quantum Hall insulators, possessing a nonvanishing charge-Hall conductance, such phases do not require a broken time-reversal symmetry. Conversely, they rely on time-reversal symmetry to guarantee spin-locked electronic propagation [1], a property that has established them as perfect candidates for magnetic-free data transportation in a large variety of spintronic applications [4].

Kramers theorem [5] governs the underlying physics of electronic insulators with \mathbb{Z}_2 -valued topological indices, guaranteeing the presence of degenerate independent spin partners, which map to each other by time-reversal symmetry. This theorem holds true for time-reversal symmetric electronic systems, associated with half-integer spins [1]. However, in classical systems, described by spinless particles (i.e., bosons), Kramers theorem does not apply [6], because the time-reversal symmetry operator \mathcal{T} squares to 1 instead of -1 , making the transposition of spin-related effects to classical wave systems highly nontrivial [3]. For this reason, approaches to achieve classical analogs of \mathbb{Z}_2 topological insulators have been based on employing additional degrees of freedom (DOFs) to form a *pseudo*-time-reversal symmetry operator \mathcal{T}_{ps} , obeying $\mathcal{T}_{\text{ps}}^2 = -1$, at the cost of implying a more stringent symmetry condition on the topological phase. For instance, electromagnetic \mathbb{Z}_2 phases have leveraged the degeneracy between transverse electric (TE) and transverse magnetic (TM) polarizations occurring in metamaterials with

$\epsilon = \mu$, enabling the formation of two degenerate pseudospin states akin to the Kramers pairs for fermions [7]. A similar strategy has been successfully implemented in the context of thin-plate elastic systems supporting Lamb waves with degenerate polarizations [8–10]. For scalar waves such as sound, however, these tricks do not work due to the lack of intrinsic polarization [11]. Instead, previously proposed strategies to realize \mathbb{Z}_2 topological phases in acoustic systems attempt to emulate Kramers pairs by exploiting other DOFs., such as crystalline symmetry. The C_{6v} point-group symmetry of hexagonal crystals, for instance, has been widely used over the last few years to achieve acoustic pseudospin, built using the high-symmetric corners of the Brillouin zone (K and K'), referred to as valleys in the literature [12–16]. By unit-cell expansion, these valleys can be folded onto the center of the Brillouin zone to achieve pseudospin states, which resemble Kramers pairs providing C_{6v} is preserved [17–20]. This approach, however, fails at inducing a rigorous \mathbb{Z}_2 topological invariant since it results in the Kramers degeneracy only at the center of the valleys, and not over the entire band. As such, in contrast to electronic quantum spin Hall phases, the edge modes of these kinds of structures are gapped [21]. In addition, the difficulties in extending \mathbb{Z}_2 topological phases to two-dimensional acoustic systems have largely hampered their exploration in higher-dimensional systems, for instance in three-dimensional sonic topological insulators and Weyl and nodal systems [22,23].

Here, we propose and demonstrate a platform to experimentally probe acoustic topological phases in higher dimensions, supporting acoustic spins with exact Kramers degeneracy. Our method allows us to explore the rich physics of sonic \mathbb{Z}_2 Weyl semimetals [24]. Remarkably, we achieve three-dimensional (3D) \mathbb{Z}_2 topological phases in a two-by-two tight-binding Hamiltonian with a single space dimension and two additional synthetic dimensions (introduced as

^{*} Author to whom correspondence should be addressed:
romain.fleury@epfl.ch

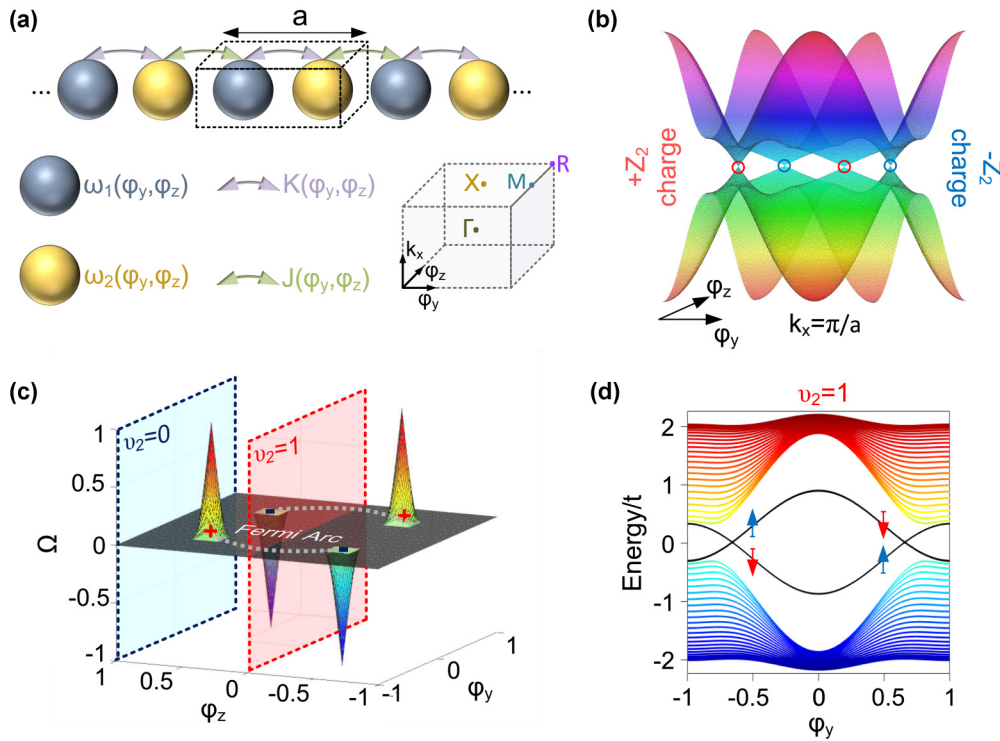


FIG. 1. Construction of a \mathbb{Z}_2 Weyl system in a two-band tight-binding system with synthetic dimensions. (a) We consider a one-dimensional tight-binding chain in which the on-site energies and hoppings depend periodically on two phason degrees of freedom, φ_y and φ_z , allowing us to define a synthetic three-dimensional momentum space, whose Brillouin zone is shown in the inset. (b) 3D band structure at the plane $k_x = \pi/a$, showing the existence of four Weyl points. (c) Berry curvature Ω of the bottom band of (b), illustrating the chiralities of the Weyl points. The figure also represents the two fixed- φ_z planes discussed in the main text, along with their \mathbb{Z}_2 topological invariants $\nu_2(\varphi_z)$. (d) Helical surface states in the \mathbb{Z}_2 topological plane $\varphi_z = \pi/4$.

parametric phason degrees of freedom). We demonstrate the construction of pairs of Weyl points [25–32] carrying \mathbb{Z}_2 topological charges in the synthetic momentum space. In order to observe the associated topological phase transitions in simple sound scattering tests, we synthesize our system in a standard acoustic pipe supporting evanescently coupled quasibound states [33–40] embedded in the continuum of the single propagating mode. Our experiments with airborne audible sound open a viable path for the experimental exploration of \mathbb{Z}_2 topological phases in dimensions higher than 2. Our findings also establish the relevance of acoustic bound states in continuum as a relevant platform for probing a variety of topological physical effects using far-field scattering tests.

II. DESIGN OF A \mathbb{Z}_2 WEYL HAMILTONIAN

We start by demonstrating how to effectively construct a \mathbb{Z}_2 Weyl system from a tight-binding chain with a single physical dimension x , and two synthetic dimensions y and z . Consider the one-dimensional tight-binding chain represented

$$H(k_x, \varphi_y, \varphi_z) = \begin{pmatrix} \omega_1(\varphi_y, \varphi_z) & K(\varphi_y, \varphi_z) + J(\varphi_y, \varphi_z)e^{-ik_x} \\ K(\varphi_y, \varphi_z) + J(\varphi_y, \varphi_z)e^{ik_x} & \omega_2(\varphi_y, \varphi_z) \end{pmatrix}. \quad (1)$$

This strategy, which allows us to interpret physical phenomena associated with a family of one-dimensional systems

in Fig. 1(a). The unit cell of the array is composed of two resonators with resonance frequencies ω_1 and ω_2 , evanescently coupled to each other with an (intracell) coupling coefficient K . The nearest-neighboring cells, on the other hand, are coupled to each other via (extracell) coupling coefficients J . The basic idea to introduce two additional synthetic dimensions is to let the physical parameters of the chain (ω_1 , ω_2 , K , and J) depend on two real parameters φ_y and φ_z . The latter, called phason degrees of freedom, will take the role of the y and z components of the Bloch wave vector in the 3D synthetic Brillouin zone, while the k_x component is the physical Bloch wave number of the one-dimensional chain. The real-valued functions $\omega_{1,2}(\varphi_y, \varphi_z)$, $K(\varphi_y, \varphi_z)$ and $J(\varphi_y, \varphi_z)$ therefore need to be periodic, e.g., with period equal to π , with respect to both phasons φ_y and φ_z , leading to the Brillouin zone represented in the inset of Fig. 1(a). Specifying the functions $\omega_{1,2}(\varphi_y, \varphi_z)$, $K(\varphi_y, \varphi_z)$, and $J(\varphi_y, \varphi_z)$ defines a family of one-dimensional systems, generated by sweeping φ_y and φ_z . The associated three-dimensional tight-binding Hamiltonian is of the form

as consequences of higher-dimensional physics, has already been exploited in a variety of prior works, for example

[41–43], although not directly in the specific form of Eq. (1). Here, we are interested in the realization of a \mathbb{Z}_2 Weyl semimetal, which we now describe.

Generally speaking, \mathbb{Z}_2 Weyl phases [24] are observed in time-reversal-invariant Weyl systems described by a tight-binding Hamiltonian that possesses two symmetries: (i) an antiunitary symmetry T such that

$$TH(k_x, \varphi_y, \varphi_z)T^{-1} = H(-k_x, -\varphi_y, -\varphi_z), \quad (2)$$

and (ii) a unitary reflection symmetry R (chosen here along z) with

$$RH(k_x, \varphi_y, \varphi_z)R^{-1} = H(k_x, \varphi_y, -\varphi_z). \quad (3)$$

The combined antiunitary operator $\tilde{T} = RT$ is also assumed to satisfy the Kramers relation $\tilde{T}^2 = -1$. Due to these symmetries, if a Weyl point is present at a particular point $(k_x^0, \varphi_y^0, \varphi_z^0)$ with a given chirality, then another one is present at $(-k_x^0, -\varphi_y^0, -\varphi_z^0)$ with the same chirality, and two other Weyl points are found at $(k_x^0, \varphi_y^0, -\varphi_z^0)$ and $(-k_x^0, -\varphi_y^0, \varphi_z^0)$ with opposite chiralities. Due to the defining properties of R and T , the following symmetry relation is always satisfied: $\tilde{T}H(k_x, \varphi_y; \varphi_z)\tilde{T}^{-1} = H(-k_x, -\varphi_y; \varphi_z)$. Therefore, the operator \tilde{T} works as time-reversal symmetry on the fixed- φ_z Hamiltonians $H(k_x, \varphi_y; \varphi_z)$, which belong to the AII class of the Atland-Zirnbauer classification of free-fermions Hamiltonians and are characterized by a \mathbb{Z}_2 index $\nu_2(\varphi_z)$. In such systems, the fixed- φ_z planes are \mathbb{Z}_2 topological planes whose topological charge can only change when crossing a gapless plane, i.e., containing a pair of Weyl points (as explained above, the Weyl points always occur in pairs on such fixed- φ_z planes). Although \mathbb{Z}_2 Weyl phases were previously reported in systems with both spin and orbital degrees of freedoms (four by four Hamiltonians), the natural spin degree of freedom is not required, and we can observe them in the simple two-by-two family of Hamiltonians of Eq. (1), providing the functions $\omega_{1,2}(\varphi_y, \varphi_z)$, $K(\varphi_y, \varphi_z)$, and $J(\varphi_y, \varphi_z)$ are properly chosen.

We start by deriving a necessary condition on these functions so that a Weyl point exists at $(k_x^0, \varphi_y^0, \varphi_z^0)$. Considering the decomposition of the Hamiltonian of Eq. (1) on Pauli matrices, $H = \frac{1}{2}(\omega_1 + \omega_2)\sigma_0 + \frac{1}{2}(\omega_1 - \omega_2)\sigma_z + (K + J \cos k_x)\sigma_x + J \sin k_x \sigma_y$, the existence of a Weyl point at $(k_x^0, \varphi_y^0, \varphi_z^0)$ requires the components of H along σ_x , σ_y , and σ_z to vanish, namely (i) $\omega_1(k_x^0, \varphi_y^0, \varphi_z^0) = \omega_2(k_x^0, \varphi_y^0, \varphi_z^0)$; (ii) $J(\varphi_y^0, \varphi_z^0) \sin k_x^0 = 0$; and (iii) $K(\varphi_y^0, \varphi_z^0) + J(\varphi_y^0, \varphi_z^0) \cos k_x^0 = 0$. The solution $J(\varphi_y^0, \varphi_z^0) = K(\varphi_y^0, \varphi_z^0) = 0$, which leads to a line node, is discarded, and the three conditions collapse to (i) $\omega_1(k_x^0, \varphi_y^0, \varphi_z^0) = \omega_2(k_x^0, \varphi_y^0, \varphi_z^0)$, (ii) $k_x^0 = \pi$, and (iii) $K(\varphi_y^0, \varphi_z^0) = J(\varphi_y^0, \varphi_z^0)$. Note that another solution is possible with $k_x^0 = 0$ but requires that the hoppings K and J be of opposite signs, which we avoid here for practical reasons.

As a second design step, we find sufficient conditions on the functions $\omega_{1,2}(\varphi_y, \varphi_z)$, $K(\varphi_y, \varphi_z)$, and $J(\varphi_y, \varphi_z)$ so that $H(k_x, \varphi_y, \varphi_z)$ satisfies the two defining symmetries R and T of \mathbb{Z}_2 Weyl systems. We assume the most natural choice for T , namely $T = K$ (K is complex conjugation). The symmetry condition of Eq. (2) then implies that the functions $\omega_{1,2}(\varphi_y, \varphi_z)$, $K(\varphi_y, \varphi_z)$, and $J(\varphi_y, \varphi_z)$ must all be chosen as even functions of (φ_y, φ_z) . Next, we need to consider

the unitary symmetry operator R . Recalling that $T^2 = +1$, while $\tilde{T} = RT$ must square to -1 , two solutions are possible. We can either pick an operator satisfying (i) $R^2 = -1$ and $[R, T] = 0$, or (ii) $R^2 = +1$ and $\{R, T\} = 0$. Picking the second option, involving a reflection that squares to 1, is the most natural choice. Since σ_y is the only Pauli matrix that anticommutes with $T = K$, we take the ansatz $R = U\sigma_y$, where U is a unitary reflection operation compatible with the above constraints (i.e., it squares to 1 and commutes with K), which can be found from Eq. (3). The symmetry condition of Eq. (3) then reduces to $H(k_x, \varphi_y, \varphi_z) = H(k_x, -\varphi_y, -\varphi_z)$, confirming that the functions $\omega_{1,2}(\varphi_y, \varphi_z)$, $K(\varphi_y, \varphi_z)$, and $J(\varphi_y, \varphi_z)$ can all be chosen as even functions of φ_z and φ_y .

Combining the periodicity and symmetry conditions mentioned above, a natural choice is to use sums of cosine functions: $\omega_1 = \gamma_y \cos \varphi_y + \gamma_z \cos \varphi_z$, $\omega_2 = -\gamma_y \cos \varphi_y - \gamma_z \cos \varphi_z$, $K = t(1 + \gamma_{xy} \cos \varphi_y + \gamma_{xz} \cos \varphi_z)$, and $J = t(1 - \gamma_{xy} \cos \varphi_y - \gamma_{xz} \cos \varphi_z)$, in which γ_y , γ_z , γ_{xy} , and γ_{xz} , t are arbitrary positive numbers. With these choices of parameters, the above-mentioned conditions for the presence of a Weyl point are satisfied at $W_1 : (k_x, \varphi_y, \varphi_z) = (\frac{\pi}{a}, \frac{\pi}{2}, \frac{\pi}{2})$. The R and T symmetries therefore imply the presence of three other Weyl points, one at $W_2 : (-\frac{\pi}{a}, -\frac{\pi}{2}, -\frac{\pi}{2}) = (\frac{\pi}{a}, -\frac{\pi}{2}, -\frac{\pi}{2})$ with the same chirality, and two others at $W_3 : (\frac{\pi}{a}, \frac{\pi}{2}, -\frac{\pi}{2})$ and $W_4 : (-\frac{\pi}{a}, -\frac{\pi}{2}, \frac{\pi}{2}) = (\frac{\pi}{a}, -\frac{\pi}{2}, \frac{\pi}{2})$ with opposite chirality.

To verify this prediction, we plot in Fig. 1(b) the 3D band structure of H for $k_x = \pi/a$, which confirms the presence of the four linear point degeneracies, symptomatic of the Weyl nodes. We also plot in Fig. 1(c) the distribution of the Berry curvature of the bottom band, confirming the opposite chiralities of the Weyl points which form sources and drains of Berry curvature, with the expected central symmetry with respect to the origin of the cut plane.

One of the most important features of \mathbb{Z}_2 Weyl phases is their gapless topological surface states supported at fixed φ_z for systems made finite along x and/or y . To determine the topology of fixed- φ_z planes, we compute their invariant $\nu_2(\varphi_z)$ using the standard formula [44,45]:

$$(-1)^{\nu_2(\varphi_z)} = \prod_{(k_x, \varphi_y) \in \text{TRIM}_2} \frac{P_f[\omega(k_x, \varphi_y; \varphi_z)]}{\sqrt{\det[\omega(k_x, \varphi_y; \varphi_z)]}}, \quad (5)$$

where the matrix ω is defined as $\omega_{ij}(k_x, \varphi_y; \varphi_z) = \varphi_i(-k_x, -\varphi_y; \varphi_z) \tilde{T} |\varphi_j(k_x, \varphi_y; \varphi_z)\rangle$, with $|\varphi_j(k_x, \varphi_y; \varphi_z)\rangle$ the wave function of the j th band, smoothly defined over (k_x, φ_y) , and TRIM_2 denotes the ensemble of momenta that are invariant under the action of \tilde{T} on the 2D cut plane.

Recalling that the invariant $\nu_2(\varphi_z)$ is a topological index and therefore cannot change unless the band gap of the cut plane closes, which happens only when the plane crosses a pair of Weyl points (at $\varphi_z = \pm\pi/2$), we calculated the invariants for two representative cut planes, namely $\varphi_z = 0$ and $\varphi_z = \pi$, represented in Fig. 1(c) in red and blue, respectively. Using Eq. (5), we find $\nu_2(0) = 1$ and $\nu_2(\pi) = 0$, which implies the presence of two helical surface states for constant- φ_z cut planes with $|\varphi_z| < \pi/2$. In real space, this means that after fixing the value of φ_z in a topological plane, for example $\varphi_z = \pi/4$, all one-dimensional chains that are finite in the x

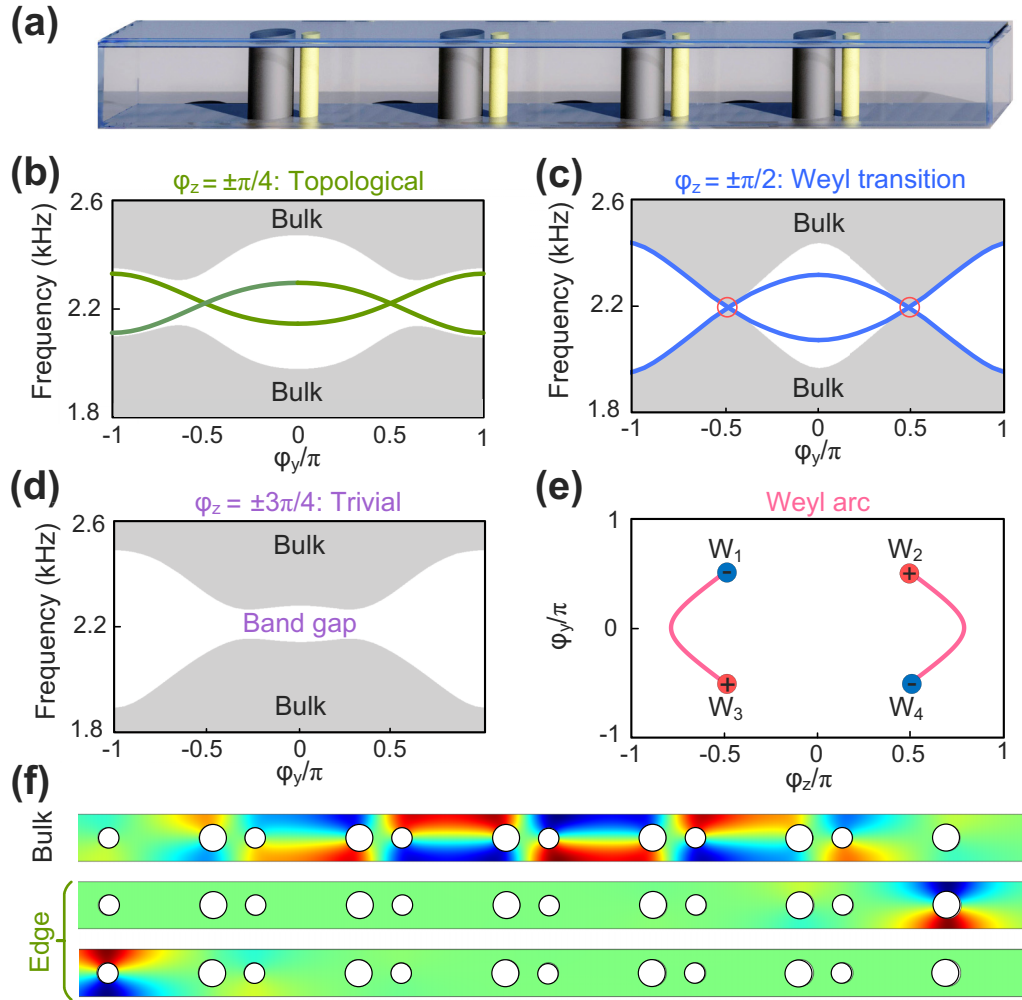


FIG. 2. Realization of a sonic \mathbb{Z}_2 Weyl system. (a) We realize a sonic \mathbb{Z}_2 Weyl system with synthetic dimensions based on the configuration shown in the inset, emulating the tight-binding toy model discussed in Fig. 1. The structure consists of an acoustic waveguide containing a one-dimensional array of cylindrical scatterers. Each cylinder of the crystal supports a bound state in the continuum (BIC). By changing the radii and the distance between the centers of the rods, the resonance frequencies and hopping amplitudes between the BICs are tuned according to the modulation scheme explained in the text. (b) Band structure of the crystal at the plane $\varphi_z = \pm\pi/4$, calculated via direct finite element simulations. The plane possesses a nonvanishing \mathbb{Z}_2 topological index. Two gap-closing helical states are observed. (c) Same as (b) but for $\varphi_z = \pm\pi/2$, which are the gapless planes at which the Weyl transition occurs. (d) Same as (b) and (c) but for $\varphi_z = \pm 3\pi/4$, which are insulating planes with zero topological charges. (e) Corresponding Fermi arcs. (f) Mode profile of one of the bulk (top) and topological helical states (bottom) at $(\varphi_y, \varphi_z) = (2\pi/10, \pi/4)$.

direction will support two 0D edge modes (located at each extremity of the 1D chain) regardless of the chosen value of φ_y . To confirm this, we plot in Fig. 1(d) the band structure corresponding to a finite 1D system of 24 unit cells at $\varphi_z = \pi/4$, showing the existence of two \mathbb{Z}_2 topological edge states, which must cross the band gap, and therefore cross each other at two specific values of φ_y . These crossing points connect the Weyl points of the \mathbb{Z}_2 system along its symmetry direction φ_z , forming the so-called Fermi arcs reported in Fig. 1(b). We note that the existence of these edge modes is protected by the pseudo-time-reversal symmetry operator \tilde{T} . As a result, any perturbation that does not break this symmetry cannot affect the insulating phase, unless its level is extremely high such that it closes the band gap (which happens at the onset of Anderson localization).

III. EXPERIMENT

We now describe the implementation of the proposed \mathbb{Z}_2 semimetal in a series of experiments that leverage the concept of synthetic dimensions. We aim at measuring both bulk and topological edge mode resonances in a noninvasive way. However, at the same time, our formulation requires a one-dimensional system of evanescently coupled acoustic resonances with easily tunable resonance frequencies and hopping rates. In particular, one must work with resonant modes that, while remaining highly localized and evanescently coupled, coexist within a radiation continuum, so that they may be externally probed. The so-called bound states in continuum (BICs) [33–40] appear to judiciously meet these requirements. In acoustics, an elegant way to exploit such bound states for

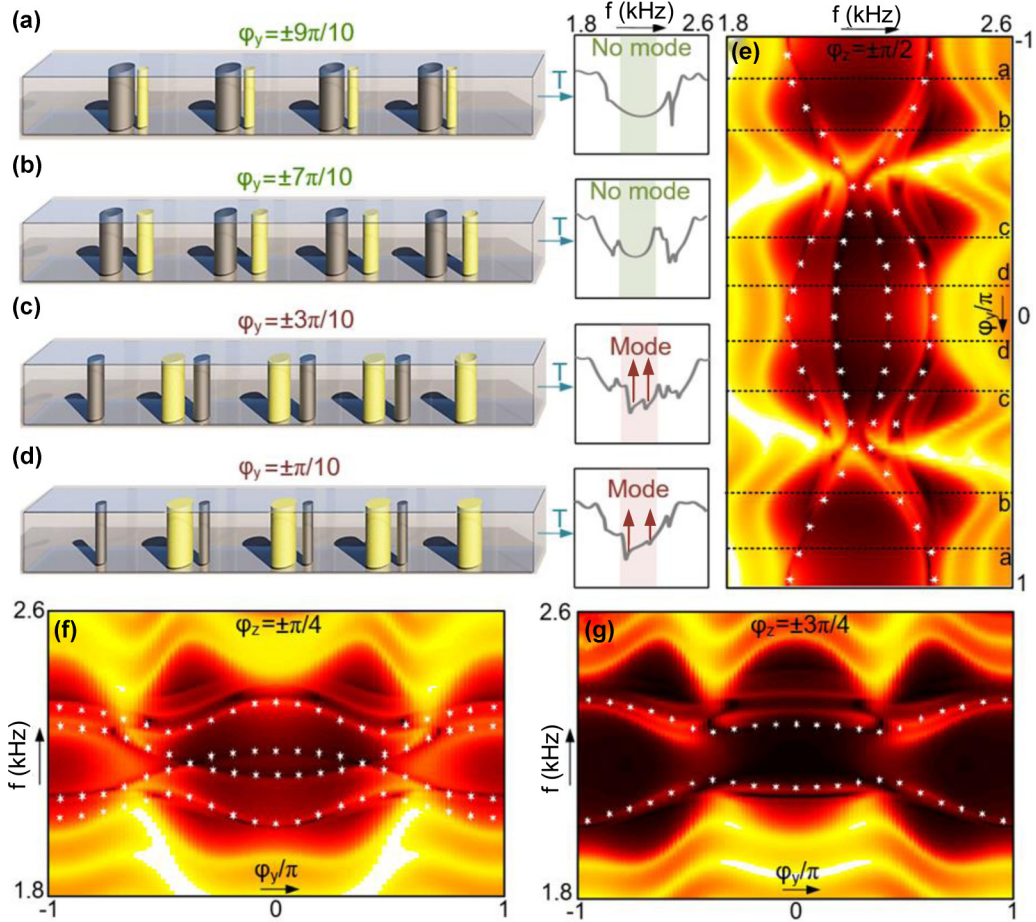


FIG. 3. Numerical demonstration of the \mathbb{Z}_2 sonic system. (a),(b) Numerically calculated transmission spectrum of the BIC chains at $\varphi_z = \pm\pi/2$, for fixed values of $\varphi_y = \pm 9\pi/10$ (a) and $\varphi_y = \pm 7\pi/10$ (b). The spectrum (shown in log scale) possesses no in-gap resonance in these cases, consistent with the dispersion diagram shown in Fig. 2(c). (c),(d) Transmission spectra at $\varphi_z = \pm\pi/2$, for $\varphi_y = \pm 3\pi/10$ (c) and $\varphi_y = \pm\pi/10$ (d). Two in-gap Fano resonances now appear in the spectrum, corresponding to the two helical surface states. (e) Continuous map of the measured transmission spectrum versus φ_y at the plane $\varphi_z = \pm\pi/2$, at which the Weyl transition occurs. (f) Same as (e) but for $\varphi_z = \pm\pi/4$, which are \mathbb{Z}_2 topological planes between the two Weyl pairs. The two gap-closing topological surface states are resolved. (g) Same as (e) and (f) but for $\varphi_z = \pm 3\pi/4$, corresponding to insulating planes with a topologically trivial band gap.

our purpose is to consider a rectangular hard-wall waveguide, which at low frequencies supports only a single propagating mode. This single-mode behavior, involving a standard acoustic plane wave, is guaranteed below the cut-off frequency ω_c of the next propagating mode, which possesses a dipolar profile in the transverse direction of the longest waveguide width. Now, consider adding a single hard-wall scatterer, in the form of a cylindrical rod, with its axis placed perpendicularly to both the propagation direction and the transverse direction of longest waveguide width, exactly in the middle of the waveguide. Notably, a discrete dipolar resonant acoustic mode exists around such symmetric obstacles, and occurs below ω_c (similar modes were discussed previously; see [46,47]). While this mode coexists in the continuum of the monopolar (plane wave) modes, it remains perfectly uncoupled from it due to the symmetry protection originating from its dipolar profile (see the Supplemental Material [48] for details). By placing next to each other several of these cylindrical obstacles, one therefore creates a chain of evanescently coupled BICs. The BIC chain has two degrees of freedom: (i) the radii of the scatterers (R_n) and (ii) the distance between them (d_n). These two parameters

map, respectively, to the resonance frequencies (ω_n) and coupling coefficients (k_n) of the two-level tight-binding model. In particular, by changing the radii of the scatterers (R_n), the resonance frequencies of the BIC modes (ω_n) can be tuned. Likewise, the distance between the resonators (d_n) determines the coupling between the nearest-neighboring sites (k_n). As a result, there is a one-to-one mapping between the sonic crystal shown in Fig. 2(a) and the tight-binding Hamiltonian of the two-level system [Eq. (1)].

Exploiting these resonances to implement the Hamiltonian of Eq. (1) for fixed values of φ_y and φ_z , we now form the corresponding family of 1D finite chains. One of these systems is schematically represented in Fig. 2(a) (this is a particular illustration with four unit cells). Each unit cell consists of two rods with different radii drawn with different colors, leading to two BIC modes with different resonance frequencies. These radii as well as the distances between the cylinders are adjusted in order to control the frequencies $\omega_1(\varphi_y, \varphi_z)$ and $\omega_2(\varphi_y, \varphi_z)$, as well as the intracell $K(\varphi_y, \varphi_z)$ and extracell $J(\varphi_y, \varphi_z)$ coupling coefficients according to the cosine laws derived previously, thereby spanning the

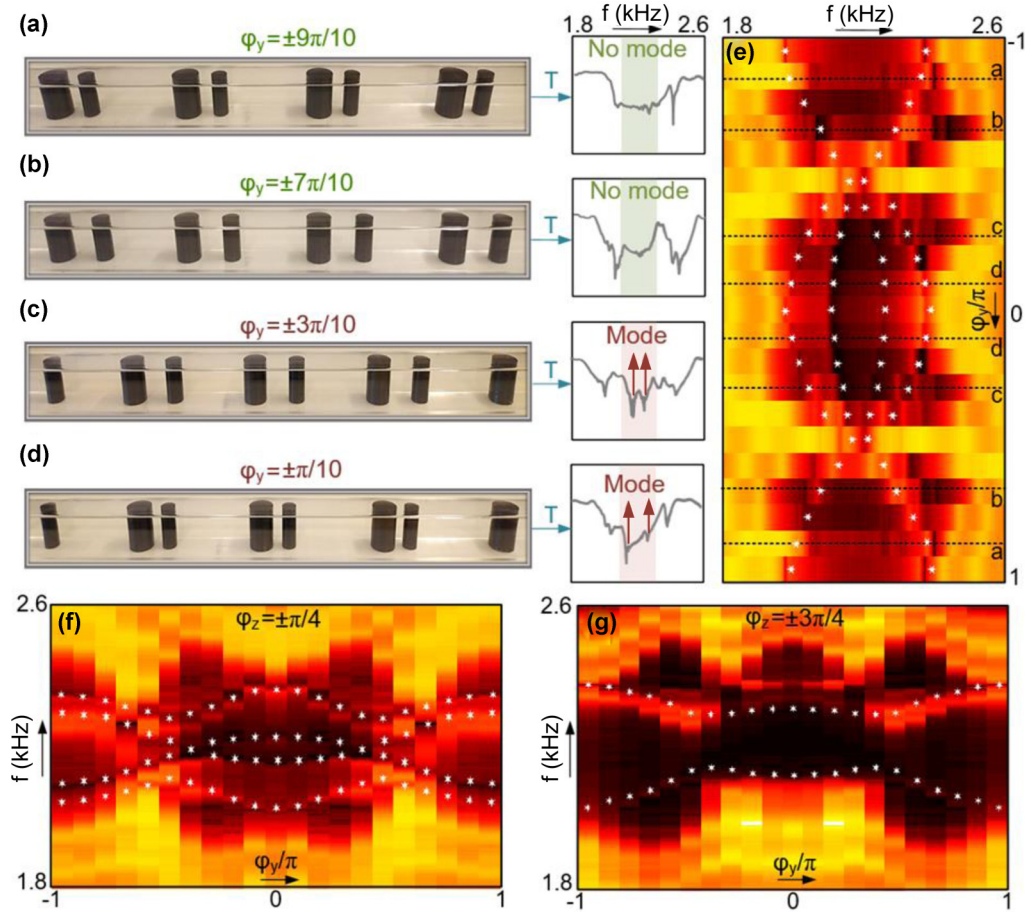


FIG. 4. Experimental demonstration of the \mathbb{Z}_2 sonic system. We construct a prototype of the proposed BIC chain. The sample consists of an acrylic square pipe, taking the role of the acoustic waveguide, and nylon cylinders with different radii, arranged inside the waveguide at specific locations. (a),(b) Measured transmission spectrum of the array at $\varphi_z = \pm\pi/2$, when φ_y is fixed at $\varphi_y = \pm 9\pi/10$ (a) and $\varphi_y = \pm 7\pi/10$ (b). Consistent with our numerical findings, no in-gap resonance exists in the recorded spectra. (c),(d) Same as (a) and (b) except that the parameter φ_y is fixed at $\varphi_y = \pm 3\pi/10$ (c), and $\varphi_y = \pm\pi/10$ (d). (e) Measured transmission spectrum of the waveguide as a function of φ_y , when φ_z is fixed at $\varphi_z = \pm\pi/2$. (f) Same as (e) but for $\varphi_z = \pm\pi/4$, corresponding to insulating planes with nonvanishing \mathbb{Z}_2 topological charges. (g) Same as (e) and (f) except that φ_z is set to be $\varphi_z = \pm 3\pi/4$. Our experimental results, being in perfect agreement with simulation, demonstrate the relevance of bound states in the continuum for exploring the rich physics of \mathbb{Z}_2 sonic system in scattering media.

synthetic momentum space. To validate the design, we performed three-dimensional full-wave simulations of the band structure, based on finite systems with six unit cells, and employing the eigenfrequency solver of Comsol Multiphysics (acoustics module).

The evolution of the numerically extracted energy spectrum versus φ_y , for different φ_z , namely $\varphi_z = \pm\pi/4$, $\varphi_z = \pm\pi/2$, and $\varphi_z = \pm 3\pi/4$, is represented in Figs. 2(b)–2(d), respectively. The lattice constant is 22.1 cm, and the transverse waveguide cross section with size 7 cm. In Figs. 2(b) and 2(d), the radius of one cylinder varies between 2 and 3.25 cm, the one of the other between 3.75 and 4.9 cm, while their separating distance changes between 4.8 and 10.9 cm. In Fig. 2(c), both radii vary between 2.9 and 4.8 cm and the separating distance in the range 7.9–14.15 cm.

At $\varphi_z = \pi/4$ [Fig. 2(b)], which is a nontrivial \mathbb{Z}_2 topological insulating plane, we confirm the presence of two helical surface states (in green). At $\varphi_z = \pi/2$, corresponding to the phase transition plane, the Weyl nodes close the band gap [Fig. 2(c)]. Finally, at the trivial plane $\varphi_z = 3\pi/4$, we

observe the expected gapped spectrum with no edge states. The behavior at all fixed φ_z is summarized in Fig. 2(e), which reports the numerically extracted Fermi arcs, consistent with the analytic results of Fig. 1(c). As a visual illustration, the profiles of the two edge modes at $(\varphi_y, \varphi_z) = (2\pi/10, \pi/4)$ is provided in Fig. 2(f), together with one of the corresponding bulk modes.

We now explain how to detect the signature of the semimetallic phases by performing a set of far-field scattering tests. As already explained, BICs are symmetry-protected and cannot radiate. As such, they cannot be excited from the far field. Yet, by slightly breaking the symmetry protecting them from radiation, the BICs can leak into the radiation continuum, allowing one to excite them from the far field using a plane-wave incident field. In order to break the underlying symmetry of our BICs (the mirror reflection symmetry of the structure), we marginally shift the cylinders away from the centerline of the waveguide, so that the BICs can couple a little bit to the waveguide mode, becoming quasi-BICs. We excite the waveguide on the left side of the system with a

plane wave, and record the transmission to the other side. We first do this numerically using finite-element simulations, including a realistic level of viscothermal losses (1.15 dB/m; see the Supplemental Material [48] for details on numerical simulations). For practical reasons linked to experimental constraints, we limit the finite system to four unit cells. We first investigate the planes $\varphi_z = \pm\pi/2$, which are the Weyl point planes. Figures 3(a)–3(e) display the numerically extracted transmission spectra recorded for different φ_y on this plane. When $\varphi_y < -\pi/2$ or $(\varphi_y > \pi/2)$ [Figs. 3(a) and 3(b)], the transmission spectrum exhibits no in-gap resonance (see shaded green area), consistent with the band structure shown earlier in Fig. 2(c). When $-\pi/2 < \varphi_y < \pi/2$, on the contrary, two successive Fano resonances appear in the spectrum [Figs. 3(c) and 3(d)] within the frequency range that was a band gap in Figs. 3(a) and 3(b). These two resonances are consistent with the presence of the two edge states. This is confirmed by the color plot of Fig. 3(e), representing the continuous evolution of the transmission spectrum versus φ_y . The results of this figure clearly indicate the presence of two topological in-gap states, when $-\pi/2 < \varphi_y < \pi/2$ (we highlight the location of spectral features corresponding to the edges of the bulk bands and the edge states with white stars). Figures 3(f) and 3(g) reproduce the results of Fig. 3(e) for the cut planes $\varphi_z = \pm\pi/4$ and $\varphi_z = \pm 3\pi/4$, corresponding to the planes with nontrivial and trivial topologies, respectively. The results of these figures are in perfect agreement with the predictions of Fig. 2.

We built samples in order to experimentally validate the topological transitions associated with the \mathbb{Z}_2 semimetallic phase (see the insets of Fig. 4). The prototypes consist of an acrylic square pipe, taking the role of the acoustic waveguide, and a set of cylindrical nylon rods with proper radii and locations. We follow the same procedure as in Fig. 3. We excite the waveguide with a loudspeaker from one side and measure the corresponding transmission coefficients at different φ_y , when φ_z is fixed at $\varphi_z = \pm\pi/2$ (see the Appendix for experimental methods). Figures 4(a)–4(d) indicate the measured transmission coefficients of the two-port system for $\varphi_y = \pm 9\pi/10$, $\varphi_y = \pm 7\pi/10$, $\varphi_y = \pm 3\pi/10$, and $\varphi_y = \pm\pi/10$. Consistent with simulations, no in-gap resonance exists in the spectrum for the first two cases [Figs. 4(a) and 4(b)]. On the other hand, when $-\pi/2 < \varphi_y < \pi/2$, the spectrum includes two in-gap Fano resonances, revealing the presence of the topological states. Figures 4(e)–4(g) represent the evolution of the transmission spectra as a function of φ_y , for the fixed values of $\varphi_z = \pm\pi/2$, $\varphi_z = \pm\pi/4$, and $\varphi_z = \pm 3\pi/4$, respectively. The results of this series of 63 independent measurements are in very good agreement with our previous numerical findings, consistent with the topology of the synthetic 3D Hamiltonian.

IV. CONCLUSION

In summary, we demonstrated, both numerically and experimentally, the realization of a \mathbb{Z}_2 acoustic Weyl system, a class of three-dimensional topological systems characterized by topological phase boundaries in momentum space, separating insulating layers with different \mathbb{Z}_2 indices. Such semimetallic phases were achieved in a 3D synthetic momen-

tum space, constructed by judiciously arranging BICs in a one-dimensional phononic crystal.

Our proposal provides a fruitful platform for the exact extension of topological insulators with a \mathbb{Z}_2 -valued topological index to various applicative fields of classical wave physics, including acoustics, optics, plasmonics, mechanics, and elastic waves. An example of such an extension to microwave systems is provided in the Supplemental Material [48]. Besides, our strategy to employ bound states in continuum for accessing the complex physics of Weyl phases opens exciting venues for further exploration of other types of topological phases of matter, simply by performing far-field scattering tests. In the Appendix, for instance, we briefly discuss the possibility of observing quantum Hall states by properly arranging sonic BICs in one dimension. In the Supplemental Material [48], the possibility of observing nodal semimetals [49,50] in our system is explained. Finally, this method also holds great promise for the realization of \mathbb{Z}_2 topological phases in dimensions higher than what is physically available.

ACKNOWLEDGMENT

This work was supported by the Swiss National Science Foundation (SNSF) under Grant No. 172487.

APPENDIX

1. Experimental methods

As a waveguide, we used an acrylic extruded clear tube with a cross section of approximately 50 cm² and a wall thickness of about 3 mm. Nylon 6 plastic cylindrical rods were radially cut at desired diameters (according to the modulation schemes prescribed in the main text), and arranged inside the waveguide. The prototype was tested in the experimental setup shown in Fig. 6 of the Supplemental Material. The setup includes a loudspeaker, a Data Physics Quattro analyzer controlled by a computer, three microphones recording sound pressure level, and an acoustic anechoic termination (not shown in the figure) preventing unwanted reflection. The loud speaker was excited with a burst noise signal. By recording the sound pressure levels measured by the microphones and employing the standing-wave pattern analysis, the transmission spectrum of the structure was extracted.

2. Observation of quantum Hall effect in sonic bound states in the continuum

In this section, we investigate the possibility of observing integer quantum Hall effect by arranging, in one dimension, sonic bound states in the continuum. We start with remarking that, in general, 2D quantum Hall phases are hard to achieve in acoustics, due to the lack of strong magnetization effects. Here, on the contrary, we show how the unique character of BICs enables probing the signature of these phases in a 1D scattering phononic crystal. We start with considering a tight-binding Hamiltonian of the form

$$H = \sum_n \omega_n a_n^\dagger a_n + \sum_n k_n a_{n+1}^\dagger a_n + \text{H.c.}, \quad (\text{A1})$$

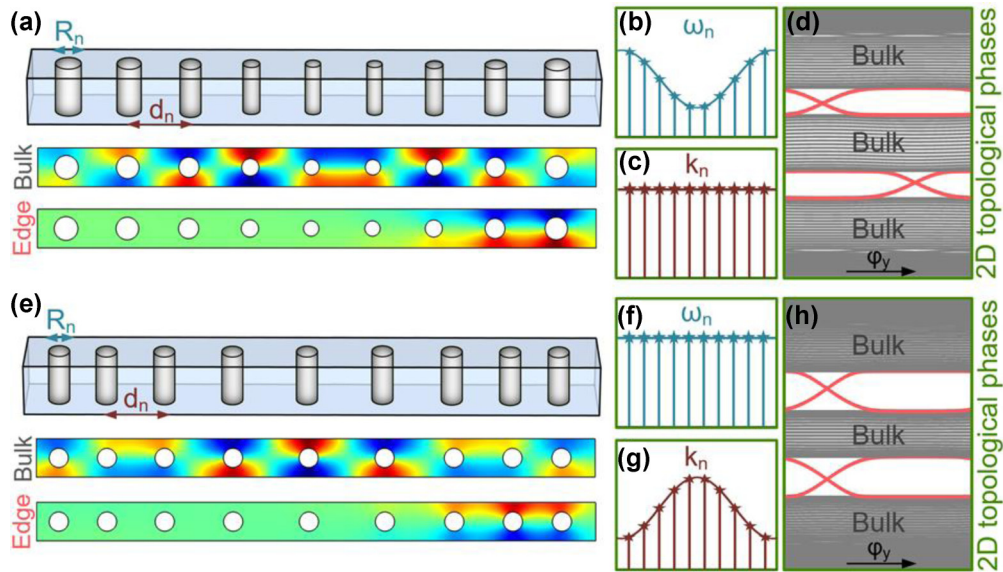


FIG. 5. Observing integer quantum Hall effect in sonic bound states in continuum. (a) A one-dimensional array of sonic BICs is implemented. (b) By varying the diameters of the rods, the resonance frequencies of the BIC states are modulated according to the relation $\omega_n = A \cos(2\pi bn + \varphi_y)$. (c) The hopping rate (k_n) between the nearest-neighbor BICs is kept constant. (d) Band structure of the crystal versus the modulation phase φ_y . The band structure includes gapless topological edge modes. (e)–(h) Same as (a)–(d) except that, this time, the on-site energies of the BICs are fixed, whereas the hopping amplitudes are modulated according to the relation $k_n = B \cos(2\pi bn + \varphi_y)$.

in which ω_n and the k_n are the on-site potentials and the hopping rates, respectively. We map this tight-binding Hamiltonian into the one-dimensional sonic BIC chain shown in Fig. 5(a), in which the resonance frequencies and hopping amplitudes are adjusted by changing the radii and the distance between the centers of the cylinders, respectively. Our aim is to realize quantum Hall phases based on the 1D tight-binding Hamiltonian given in Eq. (A1). The quantum Hall effect is a two-dimensional phenomenon. Hence, in order to observe it in one dimension, one has to introduce extra degrees of freedom. We do this by varying the on-site potentials of the BIC chain according to the algorithm $\omega_n = A \cos(2\pi bn + \varphi_y)$ [see Fig. 5(a)], in which A is the amplitude of the modulation, b sets the periodicity of oscillation, and φ_y is an arbitrary phase between $-\pi$ and π . Note that, in this case, we assume the tunneling rates k_n to be fixed, i.e., $k_n = k_0$. With these choices of parameters, the tight-binding Hamiltonian H in Eq. (A1) will be the same as the so-called Hofstadter Hamiltonian, describing the interaction of electrons with a uniform out-of-plane magnetic flux. Figure 5(d) shows the band structure of the chain as a function of the modulation parameter φ_y . It

is seen that the band structure of the crystal exhibits gapless topological edge modes, which are akin to the states emerging on the boundaries of quantum Hall systems. In the insets of Fig. 5(a), we have reported the profiles of one of the bulk and edge modes. Notice that, while the edge mode of the array is confined in zero dimensions, it flows unidirectionally along the synthetic dimension with the wave number of φ_y .

An alternative route to achieve quantum Hall phases is to embed the additional degree of freedom in the other available parameter of the tight-binding Hamiltonian, namely the hopping amplitude k_n . More specifically, instead of varying the on-site potentials of the BIC chain and keeping its hopping rates constant, we consider the dual case: we modulate the hopping amplitudes according to the relation $k_n = k_0[1 + B \cos(2\pi bn + \varphi_y)]$, and fix the values of the on-site potentials [see Figs. 5(f) and 5(g)]. Similar to the previous case, topological edge modes can be observed when continuously sweeping the parameter φ_y in the 2D synthetic Brillouin zone [Fig. 5(h)]. Figure 5(e) shows the mode profiles of one of the corresponding bulk and edge states.

- [1] C. L. Kane and E. J. Mele, Quantum Spin Hall Effect in Graphene, *Phys. Rev. Lett.* **95**, 226801 (2005).
- [2] B. A. Bernevig, T. L. Hughes, and S. C. Zhang, Quantum spin hall effect and topological phase transition in HgTe quantum wells, *Science* **314**, 1757 (2006).
- [3] A. Soluyanov and D. Vanderbilt, Wannier representation of \mathbb{Z}_2 topological insulators, *Phys. Rev. B* **83**, 035108 (2011).
- [4] T. Jungwirth, J. Wunderlich, and K. Olejník, Spin hall effect devices, *Nat. Mater.* **11**, 382 (2012).

- [5] H. A. Kramers, General theory of paramagnetic rotation in crystals, *Proc. - Acad. Sci. Amsterdam* **33**, 959 (1930).
- [6] L. Lu, J. D. Joannopoulos, and M. Soljačić, Topological photonics, *Nat. Photon.* **8**, 821 (2014).
- [7] A. B. Khanikaev, S. H. Mousavi, W. K. Tse, M. Kargarian, A. H. MacDonald, and G. Shvets, Photonic topological insulators, *Nat. Mater.* **12**, 233 (2013).
- [8] M. Miniaci, R. K. Pal, B. Morvan, and M. Ruzzene, Experimental Observation of Topologically Protected Helical Edge Modes in Patterned Elastic Plates, *Phys. Rev. X* **8**, 031074 (2018).

- [9] S. H. Mousavi, A. B. Khanikaev, and Z. Wang, Topologically protected elastic waves in phononic metamaterials, *Nat. Commun.* **6**, 1 (2015).
- [10] M. Miniaci, R. K. Pal, R. Manna, and M. Ruzzene, Valley-based splitting of topologically protected helical waves in elastic plates, *Phys. Rev. B* **100**, 024304 (2019).
- [11] X. Zhang, M. Xiao, Y. Cheng, M. H. Lu, and J. Christensen, Topological sound, *Commun. Phys.* **1**, 97 (2018).
- [12] J. Lu, C. Qiu, L. Ye, X. Fan, M. Ke, F. Zhang, and Z. Liu, Observation of topological valley transport of sound in sonic crystals, *Nat. Phys.* **13**, 369 (2017).
- [13] Z. Zhang, Y. Tian, Y. Wang, S. Gao, Y. Cheng, X. Liu, and J. Christensen, Directional acoustic antennas based on valley-hall topological insulators, *Adv. Mater.* **30**, 1803229 (2018).
- [14] C. He *et al.*, Three-dimensional topological acoustic crystals with pseudospin-valley coupled saddle surface states, *Nat. Commun.* **9**, 4555 (2018).
- [15] T. W. Liu and F. Semperlotti, Tunable Acoustic Valley-Hall Edge States in Reconfigurable Phononic Elastic Waveguides, *Phys. Rev. Appl.* **9**, 014001 (2018).
- [16] Z. Zhang, Y. Tian, Y. Cheng, Q. Wei, X. Liu, and J. Christensen, Topological acoustic delay line, *Phys. Rev. Appl.* **9**, 034032 (2018).
- [17] W. Long-Hua and X. Hu, Scheme for Achieving a Topological Photonic Crystal by Using Dielectric Material, *Phys. Rev. Lett.* **114**, 223901 (2015).
- [18] Z. Zhang, Q. Wei, Y. Cheng, T. Zhang, D. Wu, and X. Liu, Topological Creation of Acoustic Pseudospin Multipoles in a Flow-Free Symmetry-Broken Metamaterial Lattice, *Phys. Rev. Lett.* **118**, 084303 (2017).
- [19] Y. Deng, H. Ge, Y. Tian, M. Lu, and Y. Jing, Observation of zone folding induced acoustic topological insulators and the role of spin-mixing defects, *Phys. Rev. B* **96**, 184305 (2017).
- [20] S. Yves, R. Fleury, F. Lemoult, M. Fink, and G. Lerosey, Topological acoustic polaritons: robust sound manipulation at the subwavelength scale, *New J. Phys.* **19**, 075003 (2017).
- [21] A. B. Khanikaev and G. Shvets, Two-dimensional topological photonics, *Nat. Photon.* **11**, 763 (2017).
- [22] O. Türker and S. Moroz, Weyl nodal surfaces, *Phys. Rev. B* **97**, 075120 (2018).
- [23] K. Deng *et al.*, Experimental observation of topological Fermi arcs in type-II Weyl semimetal MoTe_2 , *Nat. Phys.* **12**, 1105 (2016).
- [24] T. Morimoto and A. Furusaki, Weyl and Dirac semimetals with \mathbb{Z}_2 topological charge, *Phys. Rev. B* **89**, 235127 (2014).
- [25] M. Xiao, W. J. Chen, W. Y. He, and C. T. Chan, Synthetic gauge flux and weyl points in acoustic systems, *Nat. Phys.* **11**, 920 (2015).
- [26] Z. Yang and B. Zhang, Acoustic Type-II Weyl Nodes from Stacking Dimerized Chains, *Phys. Rev. Lett.* **117**, 224301 (2016).
- [27] B. Xie, H. Liu, H. Cheng, Z. Liu, S. Chen, and J. Tian, Experimental Realization of Type-II Weyl Points and Fermi Arcs in Phononic Crystal, *Phys. Rev. Lett.* **122**, 104302 (2019).
- [28] D. Z. Rocklin, B. G. G. Chen, M. Falk, V. Vitelli, and T. C. Lubensky, Mechanical Weyl modes in Topological Maxwell Lattices, *Phys. Rev. Lett.* **116**, 135503 (2016).
- [29] V. Peri, M. Serra-Garcia, R. Ilan, and S. D. Huber, Axial-field-induced chiral channels in an acoustic Weyl system, *Nat. Phys.* **15**, 357 (2018).
- [30] T. Zhang, Z. Song, A. Alexandradinata, H. Weng, C. Fang, L. Lu, and Z. Fang, Double-Weyl Phonons in Transition-Metal Monosilicides, *Phys. Rev. Lett.* **120**, 016401 (2018).
- [31] H. Ge, X. Ni, Y. Tian, S. K. Gupta, M. H. Lu, X. Lin, W. D. Huang, C. T. Chan, and Y. F. Chen, Experimental Observation of Acoustic Weyl Points and Topological Surface States, *Phys. Rev. Appl.* **10**, 014017 (2018).
- [32] W. J. Chen, M. Xiao, and C. T. Chan, Photonic crystals possessing multiple weyl points and the experimental observation of robust surface states, *Nat. Commun.* **7**, 13038 (2016).
- [33] C. W. Hsu, B. Zhen, A. D. Stone, J. D. Joannopoulos, and M. Soljačić, Bound states in the continuum, *Nat. Rev. Mater.* **1**, 16048 (2016).
- [34] L. Carletti, K. Koshelev, C. De Angelis, and Y. Kivshar, Giant Nonlinear Response at the Nanoscale Driven by Bound States in the Continuum, *Phys. Rev. Lett.* **121**, 033903 (2018).
- [35] D. C. Marinica, A. G. Borisov, and S. V. Shabanov, Bound States in the Continuum in Photonics, *Phys. Rev. Lett.* **100**, 183902 (2008).
- [36] Y. X. Xiao, G. Ma, Z. Q. Zhang, and C. T. Chan, Topological Subspace-Induced Bound State in the Continuum, *Phys. Rev. Lett.* **118**, 166803 (2017).
- [37] H. M. Doeleman, F. Monticone, W. den Hollander, A. Alù, and A. F. Koenderink, Experimental observation of a polarization vortex at an optical bound state in the continuum, *Nat. Photon.* **12**, 397 (2018).
- [38] M. I. Molina, A. E. Miroshnichenko, and Y. S. Kivshar, Surface Bound States in the Continuum, *Phys. Rev. Lett.* **108**, 070401 (2012).
- [39] A. Kodigala, T. Lepetit, Q. Gu, B. Bahari, Y. Fainman, and B. Kanté, Lasing action from photonic bound states in continuum, *Nature (London)* **541**, 196 (2017).
- [40] K. Koshelev, S. Lepeshov, M. Liu, A. Bogdanov, and Y. Kivshar, Asymmetric Metasurfaces with High-Q Resonances Governed by Bound States in the Continuum, *Phys. Rev. Lett.* **121**, 193903 (2018).
- [41] Y. E. Kraus, Y. Lahini, Z. Ringel, M. Verbin, and O. Zilberberg, Topological States and Adiabatic Pumping in Quasicrystals, *Phys. Rev. Lett.* **109**, 106402 (2012).
- [42] D. J. Apigo, W. Cheng, K. F. Dobiszewski, E. Prodan, and C. Prodan, Observation of Topological Edge Modes in a Quasiperiodic Acoustic Waveguide, *Phys. Rev. Lett.* **122**, 095501 (2019).
- [43] X. Fan, C. Qiu, Y. Shen, H. He, M. Xiao, M. Ke, and Z. Liu, Probing Weyl Physics with One-Dimensional Sonic Crystals, *Phys. Rev. Lett.* **122**, 136802 (2019).
- [44] C. L. Kane and E. J. Mele, \mathbb{Z}_2 Topological Order and the Quantum Spin Hall Effect, *Phys. Rev. Lett.* **95**, 146802 (2005).
- [45] L. Fu and C. L. Kane, Time reversal polarization and a \mathbb{Z}_2 adiabatic spin pump, *Phys. Rev. B* **74**, 195312 (2006).
- [46] F. Zangeneh-Nejad and R. Fleury, Topological Fano Resonances, *Phys. Rev. Lett.* **122**, 014301 (2019).

- [47] T. Bobinski, A. Maurel, P. Petitjeans, and V. Pagneux, Backscattering reduction for resonating obstacle in water-wave channel, *J. Fluid Mech.* **845**, R4-1 (2018).
- [48] See Supplemental Material at <http://link.aps.org/supplemental/10.1103/PhysRevB.102.064309> for experimental observation of acoustic \mathbb{Z}_2 Weyl semimetals in synthetic dimensions.
- [49] H. C. Po, Y. Bahri, and A. Vishwanath, Phonon analog of topological nodal semimetals, *Phys. Rev. B* **93**, 205158 (2016).
- [50] A. A. Burkov, M. D. Hook, and L. Balents, Topological nodal semimetals, *Phys. Rev. B* **84**, 235126 (2011).